Estimating Three-Dimensional Cloud Structure via Statistically Blended Satellite Observations

STEVEN D. MILLER,* JOHN M. FORSYTHE,* PHILIP T. PARTAIN,* JOHN M. HAYNES,*
RICHARD L. BANKERT,+ MANAJIT SENGUPTA,# CRISTIAN MITRESCU,@
JEFFREY D. HAWKINS,+ AND THOMAS H. VONDER HAAR&

* *Cooperative Institute for Research in the Atmosphere, Colorado State University, Fort Collins, Colorado*
+ *Naval Research Laboratory, Monterey, California*
# *National Renewable Energy Laboratory, Golden, Colorado*
@ *Science Systems and Applications, Inc., Hampton, Virginia*
& *Department of Atmospheric Science, Colorado State University, Fort Collins, Colorado*

(Manuscript received 25 February 2013, in final form 26 August 2013)

ABSTRACT

The launch of the NASA *CloudSat* in April 2006 enabled the first satellite-based global observation of vertically resolved cloud information. However, *CloudSat*'s nonscanning W-band (94 GHz) Cloud Profiling Radar (CPR) provides only a nadir cross section, or ''curtain,'' of the atmosphere along the satellite ground track, precluding a full three-dimensional (3D) characterization and thus limiting its utility for certain model verification and cloud-process studies. This paper details an algorithm for extending a limited set of vertically resolved cloud observations to form regional 3D cloud structure. Predicated on the assumption that clouds of the same type (e.g., cirrus, cumulus, and stratocumulus) often share geometric and microphysical properties as well, the algorithm identifies cloud-type-dependent correlations and uses them to estimate cloud-base height and liquid/ice water content vertical structure. These estimates, when combined with conventional retrievals of cloud-top height, result in a 3D structure for the topmost cloud layer. The technique was developed on multiyear *CloudSat* data and applied to Moderate Resolution Imaging Spectroradiometer (MODIS) swath data from the NASA *Aqua* satellite. Data-exclusion experiments along the *CloudSat* ground track show improved predictive skill over both climatology and type-independent nearest-neighbor estimates. More important, the statistical methods, which employ a dynamic range-dependent weighting scheme, were also found to outperform type-dependent near-neighbor estimates. Application to the 3D cloud rendering of a tropical cyclone is demonstrated.

1. Introduction and background

Clouds give visual testimony to the unseen dynamics of the atmosphere; they are the manifestation of a complex underlying environmental state defined by distributions of temperature, moisture, stability, energy balance, and the myriad nonlinear feedback processes taking place simultaneously within all parts of the earth–atmosphere system. Clouds play an integral role in the radiative, chemical, dynamic, and thermodynamic feedback processes describing the current state of the atmosphere and its short-term evolution (i.e., weather) and long-term averages/trends (i.e., climate). Understanding these interactions and capturing them in numerical weather prediction (NWP) models, particularly in the context of climate simulations (e.g., Arakawa 1975), remain at the cutting edge of atmospheric research (e.g., Randall 1989; Ramanathan and Collins 1991; Wallace 1992; Stephens et al. 2004).

Despite clouds being among the first meteorological features to be considered scientifically (Luke Howard first classified them in 1802; see Stephens 2003), they in many ways remain a fundamental challenge to the research and operational communities who study work among them. Most NWP models consider cloud water as part of the model state vector (a prognostic variable; e.g., Tiedtke 1993; Zhao and Carr 1997) rather than as a diagnosed quantity. Given the observing system limitations of a three-dimensional global field, the analysis

Corresponding author address: Steven D. Miller, Cooperative Institute for Research in the Atmosphere, Colorado State University, Fort Collins, CO 80523-1375.
E-mail: steven.miller@colostate.edu

DOI: 10.1175/JAMC-D-13-070.1

of cloud parameters in NWP models is challenging. The need for improved cloud analyses is of particular importance to the operational community. For example, cloud vertical structure, cloud-base height (ceiling), and liquid–ice–mixed phase are key parameters to aviation.

Improving our ability to predict clouds in numerical models requires foundational advances to our knowledge of cloud microphysics, macrophysics, and spatial–temporal distribution. Environmental satellites provide the most tractable means to compiling these observations globally. However, limitations of contemporary operational environmental satellite observing systems (e.g., passive optical and microwave spectrum radiometers) to provide detailed, vertically resolved cloud information remains one of the main roadblocks to advancing our understanding of cloud processes.

Recognizing the importance of cloud vertical structure information, researchers have pushed the limits of passive sensor technology. Wang et al. (2009) estimate cirrus cloud particle size profiles based on multiple near-infrared (NIR) channels from the Moderate Resolution Imaging Spectroradiometer (MODIS; King et al. 1992) that provide sensitivity to different levels within the cloud (e.g., Platnick 2000). Based on these same NIR sensitivity principles, King and Vaughan (2012) show that hyperspectral measurements hold the potential to improve further upon the multispectral MODIS retrievals. Adopting the findings of Nakajima and King (1990), Miller et al. (2001) reconcile *CloudSat* (Stephens et al. 2002) radar-derived cirrus particle effective radii with cloud-top-biased retrievals from Geostationary Operational Environmental Satellite (GOES; e.g., Menzel and Purdom 1994). Information about the vertical distribution of cloud has also been approximated from passive microwave measurements (Pandey et al. 1983), combined microwave and infrared (Liu et al. 1995), and spectral/textural features via fuzzy logic to identify multilayered cloud (e.g., cirrus overlying low-level stratus; Baum et al. 1995). Related to the latter, Pavolonis and Heidinger (2004) present a practical multispectral technique for the daytime detection of overlapping cloud layers.

Work in 3D cloud generation (i.e., simulation of realistic cloud fields for use in radiative transfer calculations) includes the stochastic modeling of cirrus (Hogan and Kew 2005) and enlisting of rendering of stratocumulus via Fourier methods (Venema et al. 2006). In terms of geometric boundary estimates for an observed cloud distribution, Hutchison et al. (2006) offer a satellite-based method for cloud ceiling retrieval for the uppermost cloud layer predicated on a priori knowledge of cloud-top height, the column-integrated cloud water path, and a cloud-type-dependent assumption made on cloud water content. Their algorithm has been applied to the Visible/Infrared Imager/Radiometer Suite (VIIRS) on the Suomi National Polar-Orbiting Partnership (NPP) satellite, and its performance is currently being evaluated. Forsythe et al. (2000) combine GOES imager data with spatially limited surface observations of cloud ceilings to provide ceiling estimates for all clouds in the satellite field of view, using a simple bispectral (visible and infrared) cloud classification constraint and nearest-neighbor assignment. They find improvements over estimates based simply on interpolated surface observations. However, their analysis is restricted to low clouds (below ~3 km above ground level) because of limitations in the surface observation dataset.

Barker et al. (2011) estimate cloud ceilings using a radiation-similarity approach based on thermal infrared and visible channels to relate *donor* pixels (from the active sensor data) to *recipient* pixels in the surrounding scene. The column properties of the closest matching donor pixel are assigned in their entirety to the recipient column, and we adopt this terminology hereafter. Their technique produces radiatively consistent results when compared to Clouds and the Earth's Radiant Energy System (CERES; Wielicki et al. 1996) measured top-of-atmosphere broadband fluxes, and provides best results to distances of ~20 km away from the active sensor data.

The current algorithm offers a new approach to cloud-base height estimation and includes estimates of cloud water content profile, thereby converting a conventional two-dimensional cloud field to a full 3D structure of the topmost cloud layer. It does so by combining instantaneous passive and active sensor observations with globally compiled statistics relating cloud type to characteristic water content profiles and correlation of cloud-base heights. Passive sensor-retrieved cloud-top height and integrated water path constrain the 3D structure. The algorithm contains built-in uncertainty estimates, derived from the statistically derived weighting factors, and dynamically adjusts the constraints of estimate with range from the nearest active sensor information (defaulting to climatologically defined cloud geometric thicknesses at ranges beyond the ability of the algorithm to offer improved skill).

The paper is structured as follows. Section 2 provides a brief background on the National Aeronautics and Space Administration (NASA) A-Train sensors used for algorithm development and demonstration. Section 3 details the physical basis for compiling cloud-type-dependent statistics from the satellite data. The approach followed in applying these statistics to the estimation of cloud vertical structure properties is discussed in section 4, and section 5 presents examples and evaluates

performance. Section 6 concludes the paper with a summary and roadmap for future improvements to this algorithm.

2. The A-Train observing system

The 3D algorithm assumes an observing system composed of one or more sensors (remote or in situ), used in synergy to characterize geometric structure of the regional cloud field. Considering the ephemeral nature of clouds, it is imperative that the multisensor observations be matched closely in space and time. Here, we used the NASA A-Train (e.g., L'Ecuyer and Jiang 2010), so called for the early afternoon (~1330) local time ascending node. The A-Train flies in a sun-synchronous orbit (705 km altitude; 98.14° inclination), with an orbital period of ~105 min, and completes ~14.4 orbits per day. The A-Train constellation members considered in this study were *Aqua* and *CloudSat*, described briefly below.

The *Aqua* satellite includes the 36-band MODIS (King et al. 1992), providing the passive swath cloud information (i.e., cloud cover, top height, and integrated water path) for this study. *CloudSat* (Stephens et al. 2002) was used to obtain detailed cloud vertical structure over a small portion of the MODIS 2330-km-wide swath. The *CloudSat* Cloud Profiling Radar (CPR) provides vertically resolved information about cloud occurrence and properties, including cloud geometric boundaries, internal water content structure, and light precipitation. Kahn et al. (2008) provide an assessment of the performance of cloud geometric boundary information derived from *CloudSat*, *Cloud–Aerosol Lidar and Infrared Pathfinder Satellite Observations* (*CALIPSO*) lidar (Winker et al. 2003), and the Atmospheric Infrared Sounder (AIRS; Aumann et al. 2003) as a function of cloud type. CALIPSO provides information about optically thin cirrus and boundary layer clouds that the CPR can miss because of either sensitivity limitations or surface clutter, making the two sensors complementary (e.g., Haynes et al. 2005). For lack of a combined *CloudSat* + *CALIPSO* cloud-type product at the time of this research, our focus was on a CPR-only method for 3D cloud approximation. However, we note in passing that the current approach is readily extendable to *CALIPSO*.

3. Physical basis and statistical tools

This algorithm augments the work of Forsythe et al. (2000) and complements that of Barker et al. (2011), emphasizing cloud geometric boundary assignment, vertical water content profile, and extending these estimates to the limits of climatological skill (>100 km for some cloud types). It enlists detailed local cloud profile information from active sensors to approximate properties of the surrounding regional cloud field. The bases for the information transfer are statistical relationships drawn between cloud type and (i) geometric boundary, and (ii) cloud water content profile. Because passive satellite observing systems provide limited information about clouds in the vertical dimension (i.e., cloud-top height/pressure and in some cases the discernment of overlapping cloud layers), the technique can only be applied to the uppermost cloud layer observed. However, in principle it is generally applicable to observations collected both within the atmosphere and from the surface (e.g., aircraft and ceilometers).

a. Physical basis

The underpinning hypothesis of this algorithm is that regional clouds of a similar type often share similar properties of morphology (e.g., shape, size, and uniformity/heterogeneity). Cloud type can be derived objectively from multispectral satellite observations using both spectral- and spatial-based tests (e.g., Stowe et al. 1999). Cloud type is thus related to cloud radiative properties, but differs in some important ways. Foremost among these differences is the general relationship between cloud type and the underlying dynamic–thermodynamic environmental state. For a given region, the atmospheric conditions responsible for producing clouds of a particular type may represent conditions that exist well beyond the spatial scale of individual cloud elements, tied to airmass properties (e.g., Holton 1992) that vary on much broader spatial scales. The validity of this assumption may decrease with increasing distance between the locally and remotely observed clouds, and we seek here to quantify this assertion.

b. Cloud geometric boundary statistics

To understand the connection between locally observed cloud geometric boundaries (i.e., cloud top and base) and those of similar cloud types in the surrounding region, we introduce the concept of ''traces'' applied to the *CloudSat* curtain data. Figure 1 walks the reader through an example of trace construction. We begin by isolating the clouds of a given type in the *CloudSat* 2B-CLDCLASS data. Starting at a reference location and advancing along track, we compute differences between the reference cloud boundary height (e.g., green dots of Fig. 1c) and clouds of that same type found at increasing ranges from the reference location. As shown in Fig. 1d, clouds with little vertical variation produce smaller differences at long ranges from the reference location, whereas clouds exhibiting high variation produce larger

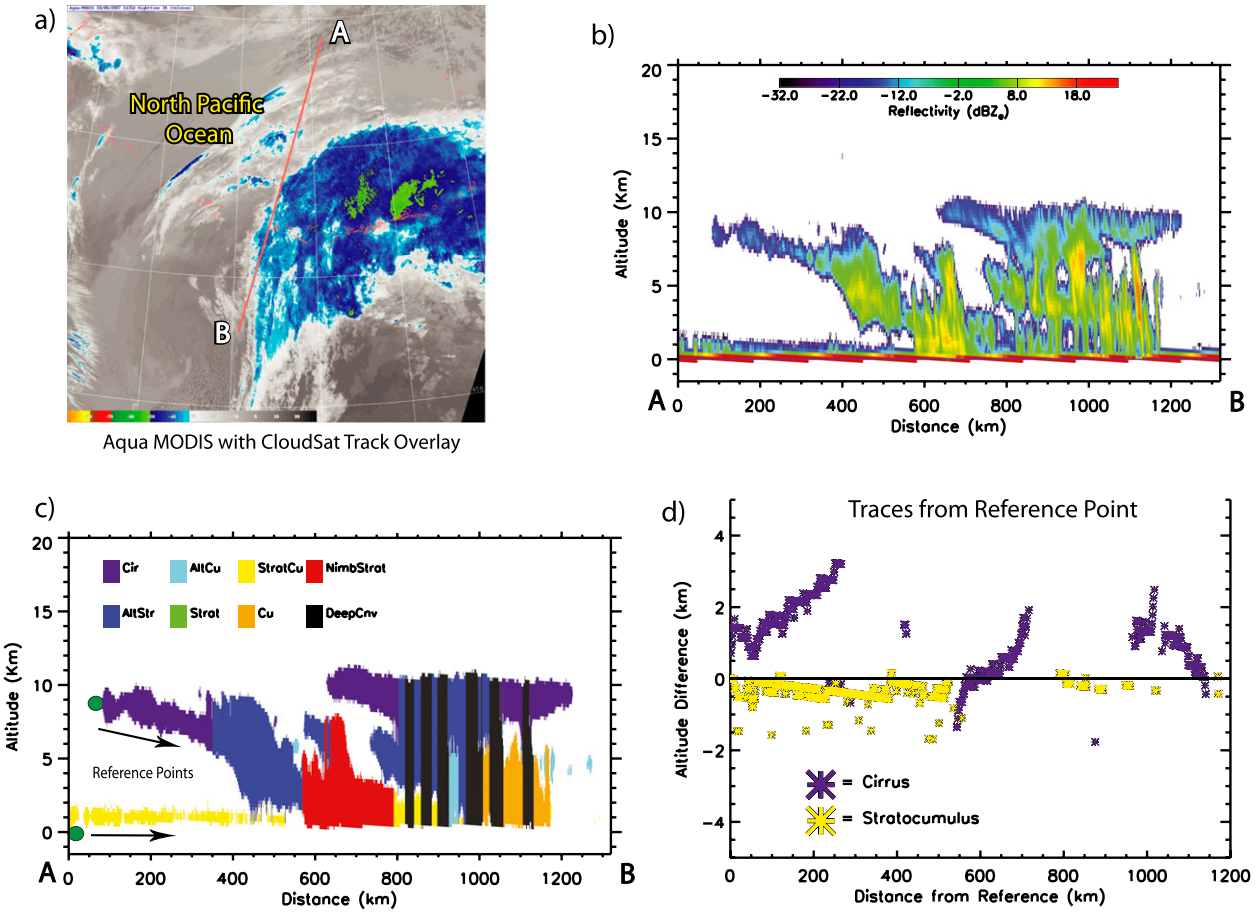

FIG. 1. Illustration of the approach to trace statistics compilation for a case over the North Pacific at 1435 UTC 8 Oct 2007: (a) *CloudSat* track overlaid on *Aqua* MODIS, (b) the CPR reflectivity profile, (c) the corresponding 2B-CLDCLASS product used to isolate clouds of different classes, with green dots designating the starting points for example cloud-base-height-difference "traces," and (d) height-difference traces computed as a function of range from the noted reference points.

differences. The geometric boundary differences, plotted as a function of range from the reference location, are referred to as traces. The ensemble of traces, shown for the examples of cirrus and stratocumulus in Fig. 2, provides a general sense for the variance of the growth of cloud boundary variability as a function of range from the reference location.

Standard deviations [$\sigma(d)$] of the difference between the reference and locally observed cloud height at distance (d) were computed from the ensemble trace statistics for cloud bases. The data were separated by cloud type [based on the 2B-CLDCLASS product: cirrus (CI), altostratus (AS), altocumulus (AC), stratus (ST), stratocumulus (SC), cumulus (CU), nimbostratus (NS), and deep convection (DC)], by latitudinal zone [bands defined as 90°–75°S (SHEM3), 75°–45°S (SHEM2), 45°–15°S (SHEM1) 15°S–15°N (TROPICS), 15°–45°N (NHEM1), 45°–75°N (NHEM2), and 75°–90°N (NHEM3)], by season [December–February (DJF), March–May (MAM), June–August (JJA), and September–November (SON)], and by surface type (land vs ocean). *CloudSat* data spanning 2006–11 were used for these statistics to provide sampling of the seasonal stratifications. In addition, we produced a global version of the statistics with no stratification.

The dependency of the global σ on range from the point of observation, as a function of seven different 2B-CLDCLASS cloud types, is shown in Fig. 3a. The curves for the various cloud types are characterized by differing rates of growth and asymptotic magnitudes. The σ curves with the smallest slope at small ranges (denoting higher correlation between heights at the reference location and nearby clouds) are CI, AC, and AS. The NS and SC type σ values grow slowly but linearly with range, while the CU and DC are nearly flat. Cloud types with smaller σ growth rates at close range tend to asymptote to larger values of σ, while cloud types with flatter curves of growth tend to reach that value quickly

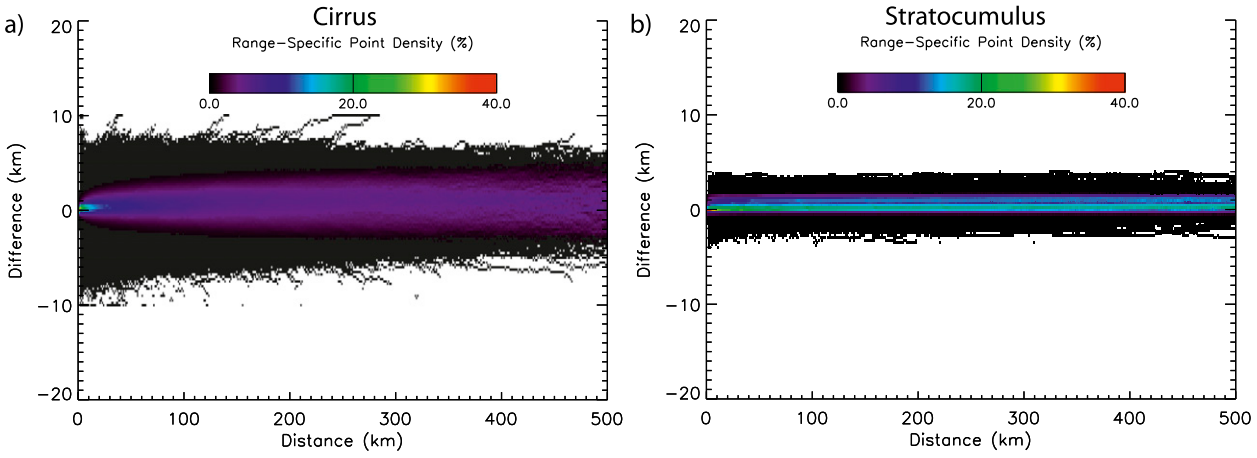

FIG. 2. The ensemble of cloud-base-height traces (e.g., building upon Fig. 1d) for the multiyear global *CloudSat* mission is used to estimate the growth of standard deviation as a function of distance from a reference point, shown here for (a) cirrus and (b) stratocumulus cloud types. The vertically confined nature of stratocumulus lends itself to a smaller standard deviation growth with distance in comparison with cirrus.

and asymptote to smaller values of σ. Small values of σ at very close range to the reference location, while not statistically significant in light of the CPR vertical resolution, provide mathematical continuity for the algorithm (to follow), which enlists these values as weighting terms.

The characteristics of these curves are largely consistent with the understood morphology attributes of these different cloud types. For example, cloud bases in the convective CU and DC types are defined by the lifted condensation level or convective condensation level, which vary slowly within a regional air mass (except near fronts or surface boundaries), and therefore σ typically is smaller. For these types, a local observation of cloud base provides a generally good predictor of the bases of other clouds in the region. Slight nonmonotonic structures of σ in the CU and DC types at ranges within ~20 km may be due to the characteristic horizontal scale of these clouds, as well as *CloudSat*'s sensitivity to precipitation, which often is associated with the DC cloud type. In contrast to the CU and DC, the σ values for the CI and AS types are relatively large. CI and AS bases appear to be more sensitive to local variations in the thermodynamic environment, and may contain small-scale morphology departures like ice fall streaks. For these clouds, a local observation of cloud base is less representative of surrounding clouds of the same type.

The curves of σ growth were decomposed by cloud type, surface type, latitudinal zone, and season. It was found that surface type (land/ocean) had little influence on σ, so only the oceanic curves were retained. Log-squared or linear curves, as appropriate, were fit to the data to provide a smooth functional relationship between σ with range. These σ values are used as weighting factors and applied to each of the donor points used to estimate the cloud-base height at a recipient point.

The fitted curves for the AC cloud type are shown in Fig. 3b, and these results are representative of the other cloud types in two important ways. First, σ was found to have significant latitudinal dependence, which is largest in the tropics and smallest at high latitudes. Second, σ tends to be largest during the warm season. Both of these effects are a direct result of the dependence of tropospheric thickness on mean temperature: in a deeper troposphere clouds have a wider range of vertical space to occupy. Therefore, a warmer–deeper troposphere will tend to have inherently larger σ values, while a colder–shallower troposphere will have a smaller σ. These fitted curves form the basis for the cloud-base-height estimation algorithm described in section 4.

c. *Defining the climatological limits of spatial correlation*

It was noted in Fig. 3 that the standard deviations reach an asymptotic value at a long range from the reference point—suggesting a climatological limit on the variation. We measured these climatological values of σ as a way of defining an upper bound to skill offered by the current approach. Potential donor clouds that reside beyond a given distance from the recipient pixel would in principle offer no skill beyond climatology. As a way of determining the climatological σ values, we produced probability density functions (PDFs) of cloud-top and cloud-base heights for each cloud type (and stratified by latitude and season). When building these PDFs, we subtracted the above-ground-level altitude from

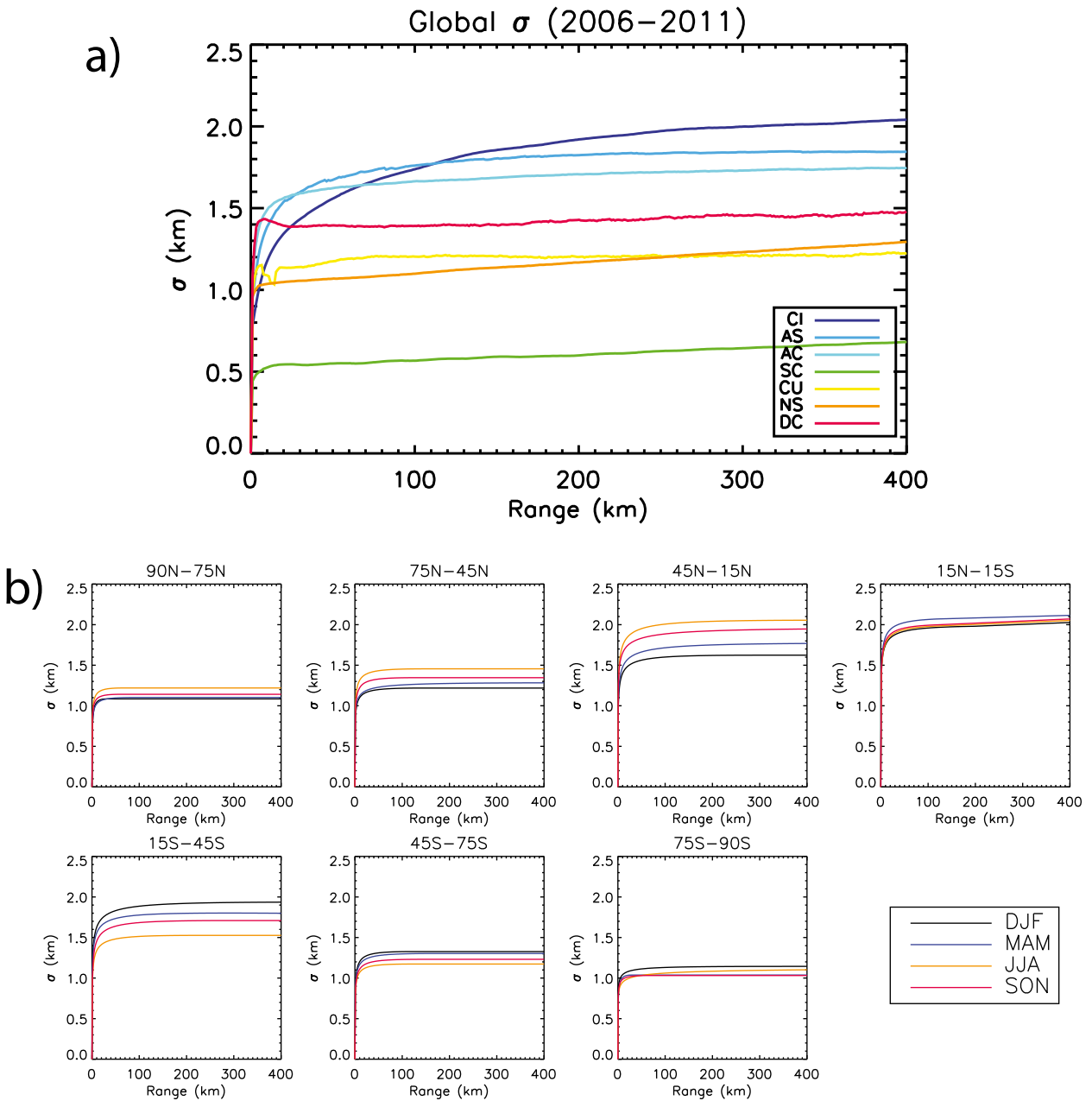

FIG. 3. (a) Global dependency of the standard deviation (σ) of cloud-base altitude on range from the point of observation, for various *CloudSat* 2B-CLDCLASS defined cloud types during 2006–2011. (b) As in (a), but fitted curves are for AC only as a function of season and zonal band.

the cloud boundary heights residing in the lower atmosphere so as to avoid increasing variance due to terrain artifacts.

We approximated normal (Gaussian) distribution fits to these PDFs by first computing the equivalent cumulative distribution functions (CDFs). The height value at the 50% level in the CDF provided the distribution's median value. We examined the absolute difference between the median height and the heights at 15.8% and 84.2% levels in the CDF to determine a standard deviation (σ). For non-Gaussian distributions, the ± 1 σ values will not be equal. The larger of the two values was chosen here to provide a conservative estimate on the width of the climatological distribution. In most cases the resultant Gaussian-equivalent PDF produced a reasonable fit to the primary mode of the observed PDFs.

By design, the asymptotic standard deviations of the trace statistics are similar to the climatological standard deviations derived here. These climatological standard deviations can be translated to an equivalent maximum range via the fitted curves (e.g., Fig. 3). Beyond this range, our method should in principle add no skill to what could be approximated by climatology. These values thus serve as an upper-bound range to the current algorithm, beyond which a climatological geometric thickness value is used for determining the cloud-base height (described below).

d. Cloud water content profile statistics

The internal structure of cloud water (i.e., liquid–ice water content) is related to cloud type via the underlying cloud formation mechanisms and airmass characteristics of the domain. We enlisted *CloudSat* data to characterize statistically the structure cloud water profile as a function of cloud type. Cloud-type-dependent vertical structures of water content, based on the *CloudSat* Level-2 Cloud Water Content product (CWC; $g\,m^{-3}$; Austin et al. 2009), were computed for the 2B-CLDCLASS cloud types. Under the assumption of a single-layer cloud, such statistics can be applied to the vertically integrated liquid/ice water content (water path; $g\,m^{-2}$), a quantity readily estimated by MODIS, to distribute this water throughout the column. Combining the estimate of cloud thickness with this vertical structure information provides an additional level of realism to the 3D estimates attempted here. A caveat to this application exists for multilayered cloud systems, wherein the MODIS-retrieval cloud water path represents the entire column as opposed to just the topmost cloud layer.

The *CloudSat* CWC product was composited to create statistical profiles versus normalized location within the cloud. To construct these profiles for a given cloud type, we first normalized the *CloudSat*-observed cloud-base and cloud-top heights (base = 0; top = 1). Next, we interpolated the observed CWC profiles to a set of 21 evenly spaced (i.e., 0.05 spacing in normalized height units) vertical bins. The interpolated cloud liquid water content for was accumulated at each vertical bin and subsequently divided by the maximum accumulation value in the column to obtain a normalized distribution. As with the cloud geometric boundary trace statistics, the climatology of CWC profile was partitioned by 2B-CLDCLASS type, season, and latitudinal zone.

Example distributions of CWC profiles for DJF and JJA seasons, overland from 15° to 45°N, are shown in Fig. 4. CU and SC have the most liquid water near cloud base (potentially rain/drizzle contaminated), while DC, AS, AC, and CI maximize CWC in midlevels of the cloud. Whereas the shapes of the curves remain similar from winter to summer, the peaks move toward slightly higher in-cloud levels in summer particularly for the convective cloud types. It is worth noting that the *CloudSat* CWC product contains known positive biases (e.g., Woods et al. 2008) due in part to the sensitivity of the measurements to precipitation-sized hydrometeors. These statistics are used here as a cloud-type-dependent template for distributing the passively retrieved integrated cloud water path between the top and base of the cloud. The current algorithm is not limited to using *CloudSat*-derived information; alternative estimates for type-dependent CWC profiles (from measurement campaigns; e.g., Brenguier et al. 2000; Lynch et al. 2002) could be applied within the current algorithm to provide improved representation.

e. Cloud geometric thickness statistics

To approximate cloud-base height in situations where no suitable donor information is available, statistics on cloud-type-dependent geometric thickness were produced from the *CloudSat* full-mission data. The geometric thickness was defined as the difference between the top and base heights for a vertically contiguous cloud layer. The results were compiled to form PDFs, assuming the same set of stratifications (cloud types, season, and latitudinal zone) used for other statistics. There was a small subset (<2% of all cloud profiles considered) of vertically contiguous layers that changed their type part way through the profile, typically occurring in regions of weak cloud detection, as explained in the 2B-CLDCLASS documentation (Wang and Sassen 2007). The three most frequently occurring in-cloud transitions of this type are from CI to AS, AS to AC, and AS to NS. In these cases the base of the upper cloud layer was truncated at the type change interface.

Table 1 summarizes the cloud geometric thickness PDF statistics. Mean, mode, and standard deviations are based on Gaussian fits to those PDFs, using the same method used to determine the climatological σ estimates described above. The strongest variations in mean thickness correspond to latitudinal zonal stratification and the convective–precipitating cloud types (likely related to the zonally dependent depth of the troposphere). The CU type exhibits a distinct seasonal dependence, with general increases in standard deviation during the spring and summer months of both hemispheres. The boundary layer-confined SC and geometrically thin AC and CI types exhibit only small variations across season and zonal band.

Although many of the features noted in Table 1 are intuitive, it was not possible to obtain such global cloud geometric thickness climatology data prior to the advent of active sensors on the A-Train. The multiyear result

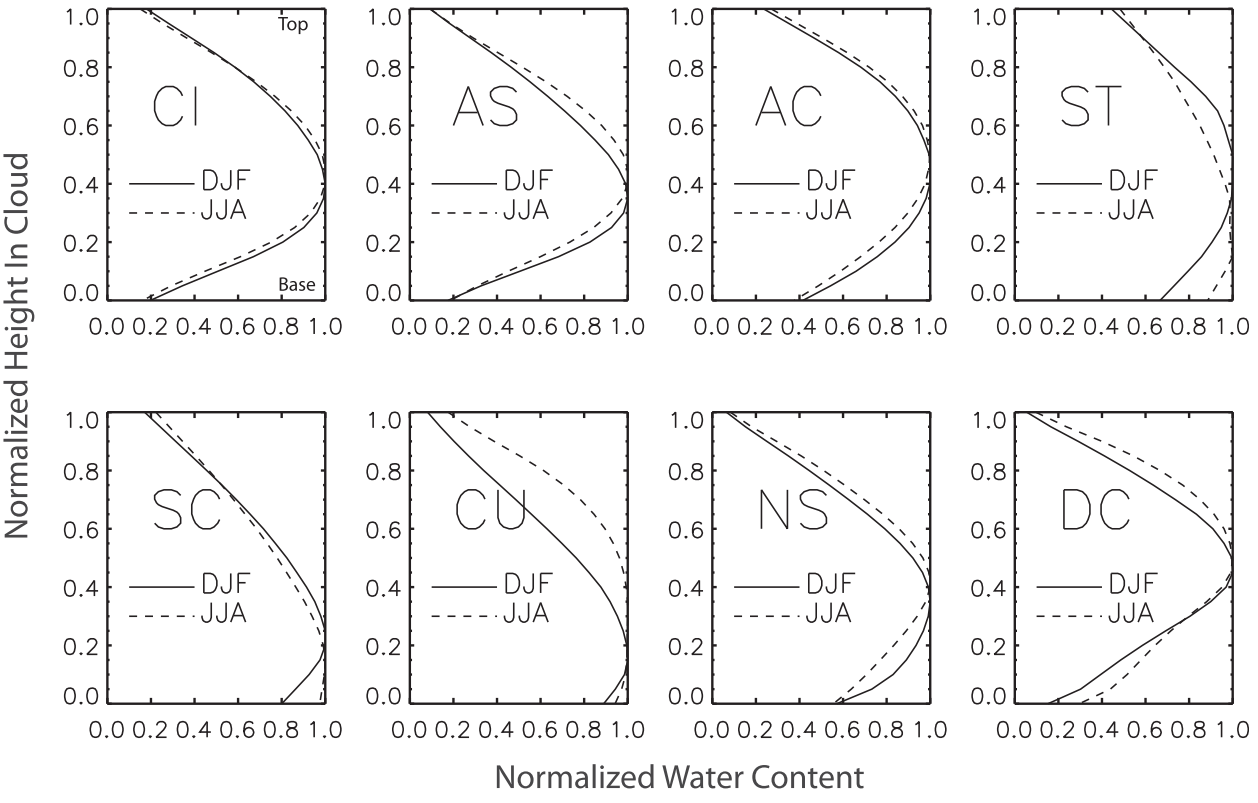

FIG. 4. Normalized cloud water content profiles for the eight 2B-CLDCLASS types, shown for midlatitude Northern Hemisphere (15°–45°N) summer and winter seasons (JJA and DJF, respectively) over land surfaces. Statistics are based on the uppermost cloud layer encountered in the profile.

shown here is a first attempt to quantify this information. We apply these results in the current algorithm to expand the estimates of cloud-base height to an arbitrarily large regional domain (wherein a subset of estimates made in that domain will be improved over climatology via the current algorithm, and the climatological geometric thicknesses can be used elsewhere). In a broader sense, the statistics could be useful to other interests, such as evaluating model-produced cloud geometric thickness climatology.

4. Algorithm description

Using the physical basis and algorithm tools developed in section 3, we conducted a series of experiments to test the hypothesis that cloud-type-constrained cloud-base estimates outperform simple nearest-neighbor methods. Algorithm performance was evaluated along the *CloudSat* ground track, using data-exclusion windows of varying size to provide built-in validation.

a. Estimation techniques

In these experiments, only the uppermost cloud layers were considered (consistent with the limitations of passive satellite observing systems), and the 2B-CLDCLASS product was used to define cloud type. Estimates were made at the recipient locations, and the *CloudSat*-observed cloud-base heights at these locations were used as truth. A data-exclusion distance between donors and the recipient was enforced to simulate the prediction of a cloud base at arbitrary locations off the *CloudSat* track. After each prediction, the recipient location was translated 50 *CloudSat* profiles (~55 km horizontal distance) forward along the *CloudSat* ground track and a new estimate was made.

A total of five cloud-base-height estimation techniques were considered here:

1) Using the cloud-base height of the *nearest neighbor* of *any* cloud type. This is the most straightforward (and presumably, least skillful) method.
2) Using the cloud-base height of the *nearest neighbor* of the *same* cloud type. This provides a direct comparison against Forsythe et al. (2000).
3) Using *climatology*-based cloud geometric thickness, based on the seasonally and zonally stratified analysis shown in Table 1. Here, the cloud-base height at the recipient location is obtained by subtracting the mean

TABLE 1. Cloud-class-dependent climatology statistics on geometric cloud thickness (km) derived from *CloudSat* data. Mean (μ), mode (M), and standard deviation (σ) are shown for each cloud type considered.

Geometric cloud thickness		AC			AS			CI			CU			DC			NS			SC		
		μ	M	σ	μ	M	σ	μ	M	σ	μ	M	σ	μ	M	σ	μ	M	σ	μ	M	σ
NHEM3	All	1.7	1.2	0.8	2.8	1.7	1.4	1.5	1.2	0.7	2.2	0.5	1.5	6.8	6.0	1.5	4.7	3.1	1.8	1.1	0.5	0.6
	DJF	1.7	0.5	0.9	2.5	1.4	1.2	1.3	1.2	0.5	1.5	0.5	0.5	7.2	8.6	1.4	4.5	3.1	1.7	1.2	0.5	0.6
	MAM	1.6	1.0	0.7	2.7	1.7	1.3	1.4	1.2	0.5	1.5	0.5	0.6	6.5	6.5	1.0	4.5	3.1	1.7	1.1	0.5	0.5
	JJA	1.8	1.2	0.8	3.3	2.2	1.4	1.7	1.2	0.7	2.8	1.0	1.9	6.8	6.0	1.5	5.2	4.8	1.9	1.0	0.5	0.5
	SON	1.7	1.2	0.8	2.9	1.7	1.4	1.5	1.2	0.6	2.2	0.5	2.4	6.6	5.8	1.5	4.7	3.4	1.8	1.1	0.7	0.5
NHEM2	All	1.7	1.2	0.8	3.2	2.2	1.5	1.8	1.2	0.8	3.1	3.4	1.5	8.2	9.8	2.5	5.3	3.4	2.1	1.1	0.7	0.6
	DJF	1.6	1.0	0.8	2.9	1.7	1.4	1.7	1.2	0.7	2.8	2.6	1.5	8.1	9.8	2.4	5.0	3.1	2.0	1.2	1.0	0.6
	MAM	1.7	1.0	0.8	3.1	1.9	1.5	1.7	1.2	0.7	3.0	3.1	1.5	7.7	6.5	2.1	5.1	3.4	2.0	1.2	0.7	0.6
	JJA	1.9	1.2	0.8	3.7	2.4	1.7	1.9	1.2	0.8	3.3	3.4	1.5	8.3	9.6	2.6	6.0	4.8	2.3	1.0	0.5	0.5
	SON	1.7	1.2	0.8	3.3	2.2	1.6	1.8	1.2	0.8	3.0	3.4	1.5	8.3	9.8	2.6	5.3	3.4	2.2	1.1	0.7	0.5
NHEM1	All	1.8	1.2	0.8	4.0	2.4	2.0	2.2	1.2	1.0	3.0	2.6	1.5	9.7	10.8	3.2	5.5	3.4	2.3	1.1	0.5	0.6
	DJF	1.7	1.2	0.8	3.7	2.2	1.7	2.1	1.2	1.0	2.9	2.6	1.4	8.8	10.6	2.7	5.2	3.4	2.1	1.2	1.0	0.6
	MAM	1.8	1.2	0.8	3.9	2.2	1.9	2.2	1.2	1.0	3.0	2.6	1.5	9.2	10.8	2.9	5.7	3.4	2.4	1.1	0.5	0.6
	JJA	2.0	1.2	0.8	4.5	2.4	2.3	2.3	1.4	1.1	3.2	3.1	1.7	10.3	12.5	4.0	6.0	3.4	2.6	1.0	0.5	0.5
	SON	1.9	1.2	0.8	4.2	2.4	2.1	2.3	1.2	1.0	3.0	2.6	1.6	9.9	11.3	3.3	5.4	3.4	2.3	1.2	0.5	0.6
TROPICS	All	2.0	1.0	0.9	5.3	6.0	2.8	2.4	1.4	1.1	3.3	2.9	1.7	11.0	13.7	4.2	6.8	3.1	3.5	1.1	0.5	0.6
	DJF	2.0	1.0	0.9	5.3	2.9	2.8	2.4	1.4	1.1	3.3	2.9	1.7	10.9	13.4	4.4	6.7	3.1	3.3	1.2	0.5	0.6
	MAM	2.0	1.0	0.9	5.3	5.8	2.8	2.4	1.4	1.1	3.3	2.9	1.7	11.0	13.7	4.3	7.3	3.1	3.5	1.2	0.5	0.6
	JJA	2.0	1.0	0.9	5.3	6.2	2.9	2.4	1.4	1.1	3.2	2.6	1.6	11.0	13.4	4.1	6.4	3.1	3.5	1.1	0.5	0.5
	SON	2.0	1.0	0.9	5.4	6.0	2.8	2.4	1.4	1.1	3.3	2.9	1.8	11.0	13.7	4.2	7.0	3.1	3.5	1.1	0.5	0.5
SHEM1	All	1.8	1.0	0.8	4.3	2.4	2.1	2.2	1.4	1.0	2.9	2.6	1.4	9.5	11.0	3.0	6.0	3.4	2.7	1.1	1.0	0.5
	DJF	1.9	1.0	0.8	4.7	2.6	2.3	2.3	1.4	1.1	3.1	2.6	1.5	10.1	11.8	3.4	6.1	3.4	2.9	1.1	0.7	0.5
	MAM	1.8	1.0	0.8	4.5	2.6	2.2	2.3	1.4	1.0	2.9	2.6	1.3	9.6	11.3	3.2	5.9	3.4	2.7	1.1	1.0	0.5
	JJA	1.7	1.0	0.8	4.1	2.4	2.0	2.2	1.2	1.0	2.8	2.4	1.3	8.7	10.6	2.7	5.9	3.4	2.7	1.1	1.0	0.5
	SON	1.8	1.2	0.8	4.2	2.4	2.0	2.2	1.2	1.0	2.9	2.4	1.3	9.3	10.8	2.9	6.0	3.4	2.7	1.1	1.0	0.5
SHEM2	All	1.7	1.0	0.8	3.3	1.9	1.6	1.8	1.2	0.8	2.9	2.9	1.5	8.2	10.1	2.5	5.5	3.4	2.3	1.1	0.7	0.5
	DJF	1.7	1.2	0.8	3.4	2.2	1.6	1.8	1.2	0.8	2.9	2.9	1.5	8.3	10.6	2.6	5.4	4.1	2.1	1.1	0.7	0.5
	MAM	1.7	1.0	0.8	3.3	1.9	1.6	1.8	1.2	0.8	2.9	2.6	1.4	8.2	9.8	2.5	5.4	3.4	2.2	1.1	0.7	0.5
	JJA	1.6	1.0	0.7	3.2	1.7	1.6	1.8	1.2	0.8	2.9	2.6	1.4	7.8	6.5	2.3	5.5	3.4	2.4	1.1	0.7	0.5
	SON	1.7	1.0	0.8	3.3	1.9	1.7	1.8	1.2	0.8	2.9	2.6	1.5	8.1	6.5	2.4	5.6	3.4	2.4	1.1	0.7	0.5
SHEM3	All	1.6	1.0	0.8	1.9	1.2	1.0	1.2	1.2	0.5	1.9	0.5	1.5	6.5	6.5	1.2	4.1	3.1	1.4	1.2	0.5	0.6
	DJF	1.6	1.0	0.8	2.0	1.2	1.0	1.2	1.0	0.5	1.8	0.5	0.8	6.2	6.5	1.0	4.0	3.1	1.3	1.1	0.5	0.6
	MAM	1.6	1.0	0.8	1.9	1.2	0.9	1.2	1.2	0.5	2.2	0.5	2.7	8.6	8.4	0.4	4.1	3.1	1.4	1.2	0.5	0.7
	JJA	1.7	0.5	0.9	1.9	1.2	0.9	1.3	1.0	0.5	2.0	0.5	2.2	—	0.0	—	4.3	3.1	1.5	1.2	0.5	0.6
	SON	1.7	0.5	0.9	2.0	1.2	1.0	1.2	1.2	0.5	1.8	0.5	1.5	8.0	8.2	0.6	4.2	3.1	1.6	1.2	0.5	0.6

geometric thickness from the radar-derived cloud-top height.

4) A distance-weighted estimate based on all points available in the donor point set. This method is referred to as *maximum donors.*
5) A distance-weighted estimate created from a *limited set* of donor points in the same cloud type as the recipient. This method is referred to as *few donors.*

In all cases involving donor points, 400 km was the greatest range allowed for a donor point to contribute information to a recipient. This is near or beyond the asymptotic climatological limits shown in Fig. 3a. The nearest-neighbor techniques are considered the benchmark upon which to assess any improvement of skill, and the *CloudSat*-derived *climatology* is a simple method that may or may not add value. The cloud-type-constrained few donors and maximum donors techniques, which embody the new algorithm developed in this research, are described below.

b. Maximum donors

The *maximum donors* technique selects all of the points along the *CloudSat* track that share the same cloud type as the recipient, starting from the minimum exclusion distance out to a maximum allowed distance of 400 km on either side of the recipient. A distance-weighted average is applied, which is a function of the spatial variability analysis in section 3. The weighting function is

$$W(d) = 1/\sigma(d)^2, \tag{1}$$

where d is the distance in kilometers from the recipient and $\sigma(d)$ is the cloud type, latitude zone, and

season-dependent standard deviation from the curve fits (e.g., Fig. 3b). The estimated cloud-base height (for example) at the recipient is formed by

$$H_b = \sum_{i=1}^{N} H_b(i)W(d_i) \Big/ \sum_{i=1}^{N} W(d_i), \qquad (2)$$

where $H_b(i)$ is the measured cloud-base height at donor point i. Since $\sigma(d)$ grows with increasing distance, this weighting scheme assigns less impact on the final estimate from more distant donor points. Cloud types with inherently higher cloud-base variability (e.g., CI, AS, and AC) have less impact at a given range than cloud types exhibiting lower spatial variability (e.g., NS, SC, DC, and CU).

c. Few donors

The few donors technique uses the same spatial weighting as maximum donors, but the number of donor points is dynamically limited. Few donors seeks to increase the contribution weight of observations at closer range. It is effectively a hybrid between maximum donors and nearest neighbor, constrained by the subset of neighbors sharing the same cloud type and allowing for more than one donor. It was hypothesized that this hybrid approach would yield a better prediction, especially at small exclusion distances and for spatially variable cloud types.

The dynamic threshold for assigning the number of donor points to consider in a given estimate of cloud-base height at a recipient point was determined as follows. By inspection of the standard deviation curves (e.g., Fig. 3a), we determined the distance at which the spatial variability curves reached their asymptotic limits. These values were determined for cloud types CI, AS, AC, SC, CU, NA, and DC as 280, 300, 250, 100, 300, 300, and 300 km, respectively. We also determined for each cloud type the standard deviation at a range of 1 km ($\sigma_{1\text{km}}$) from the trace curve as in Fig. 3b, selected by season, and latitudinal zone. After determining the geometric distance d between the recipient and nearest *CloudSat* donor point of the same cloud type, we computed the minimum number of donor points required for a few donors estimate as

$$n_{\text{Min}} = \text{maximum}(\sigma(d)/\sigma_{1\text{km}}, 2). \qquad (3)$$

At close proximity to the donor pixel, $\sigma(d)$ converges toward $\sigma_{1\text{km}}$ and the ratio approaches unity, implying usage of the two *nearest neighbor*s. The minimum of 2 donor points (as opposed to only 1) was chosen to add skill for the case of a sloping cloud base with donor points that may straddle the recipient point. As distance increases, $\sigma(d)$ increases toward the climatology value, which is larger than $\sigma_{1\text{km}}$. The ratio of these two quantities as defined in Eq. (3) thus becomes greater than 2, and so we progressively relax the few donors requirement in favor of enlisting a larger number of donors.

Uncertainty in the nearest neighbor (any cloud type) can be considered as the standard deviation of the distribution of all cloud heights in the troposphere, for that latitude zone and season. Uncertainty in climatology comes from either the standard deviations of the cloud-base height distributions or from the geometric thickness statistics of each cloud type. Uncertainty in the maximum donors and few donors are estimated objectively as the average of the range-dependent standard deviations of the donor pixels. Here, a prediction using more distant donors would have higher uncertainty since the standard deviations (e.g., Fig. 3) grow with increasing distance from the recipient.

5. Results

We begin the evaluation by considering a case study, expand to a statistical evaluation, and finally present enhanced applications.

a. Case study illustration

Figure 5 illustrates cloud-base-height predictions from the various estimation methods outlined above over the North Pacific on 8 October 2007, for a scene spanning a horizontal distance of 1300 km. *CloudSat*-derived cloud types from the top of the clouds extending to the base are color coded. The SC type occurs at the north end of the domain. An area of CI extends northward from deeper clouds classified as AS and DC.

For this example, a data-exclusion distance of ±80 km was selected. Several characteristics and limitations of each estimation method are revealed. All methods except nearest neighbor of any cloud type perform well for the low SC cloud located between 0 and 100 km along track, as well as for DC. These clouds display a more horizontally consistent base height, as was seen in Fig. 3. Climatology tends to underestimate the base of the AS clouds. The maximum donors method shows the effects of multidonor smoothing and is slow to vary within a given cloud type, while in contrast the few donors method changes more rapidly. The geometrically thick clouds residing between 800 and 1000 km along the track, alternating between AS and DC designation, presented a challenge to all four methods. This speaks to the need for quality-controlled cloud-type information, considered here as a priori input to the algorithm. All

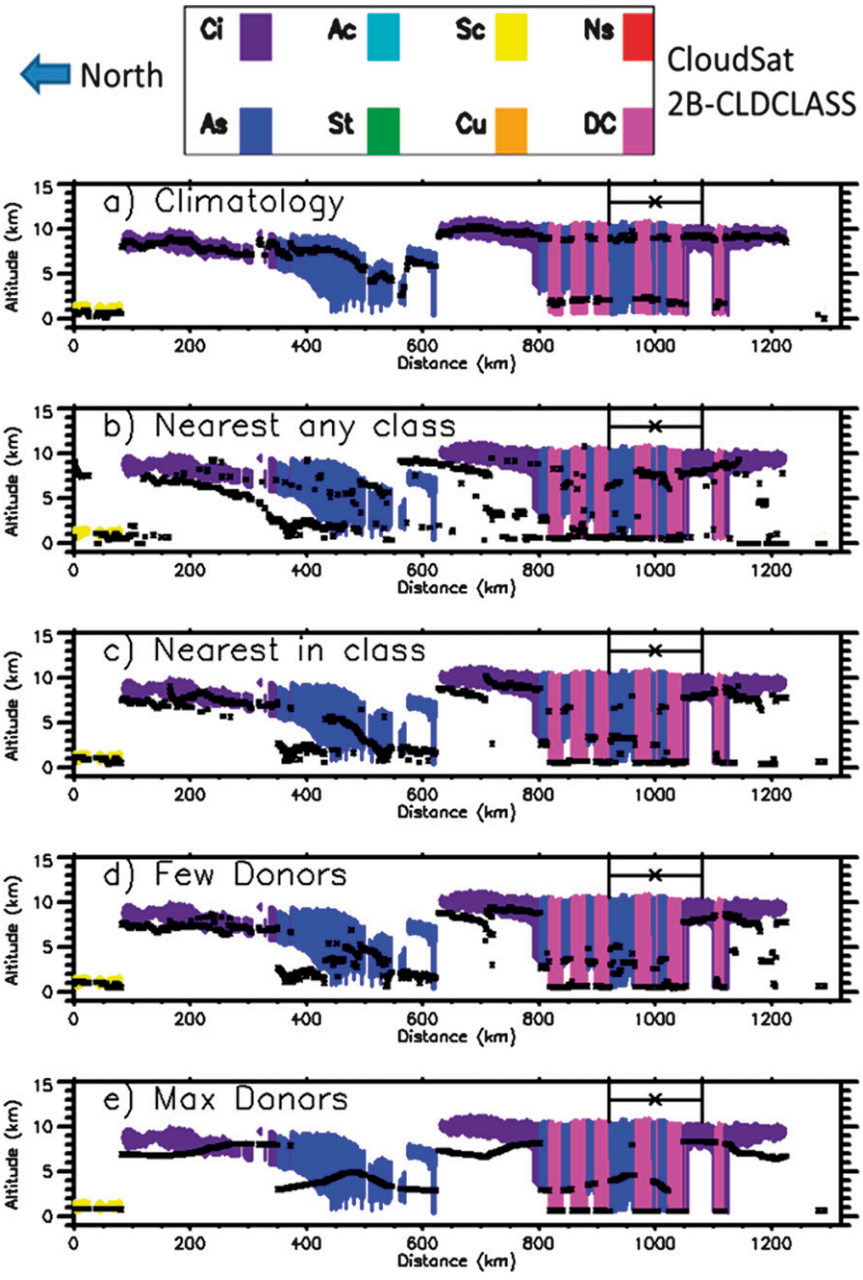

FIG. 5. Cloud-base predictions (black points) for a frontal system in the North Pacific (8 Oct 2007; *CloudSat* granule 7692). The *CloudSat* 2B-CLDCLASS is indicated by the colors. An exclusion distance of ±80 km was used, as illustrated by the distance bar from the recipient point ×, plotted for example at 1000 km. Only the uppermost, radar-detected base and top are shown.

methods performed well for DC, particularly for the few donors and maximum donors techniques.

b. Multiyear global statistics

To assess performance statistically, the data-exclusion experiments were repeated for four years of July (2007–10), using data from 50°N to 50°S. The correlation and root-mean-square (RMS) error between the estimates and the truth base value at the recipient location were calculated. The data-exclusion experiment was run at four arbitrarily selected exclusion windows: 20, 60, 100, and 200 km. In this experiment, no cloud-base estimate was allowed to exceed the radar-indicated top of the cloud. Such an unphysical condition would unfairly penalize

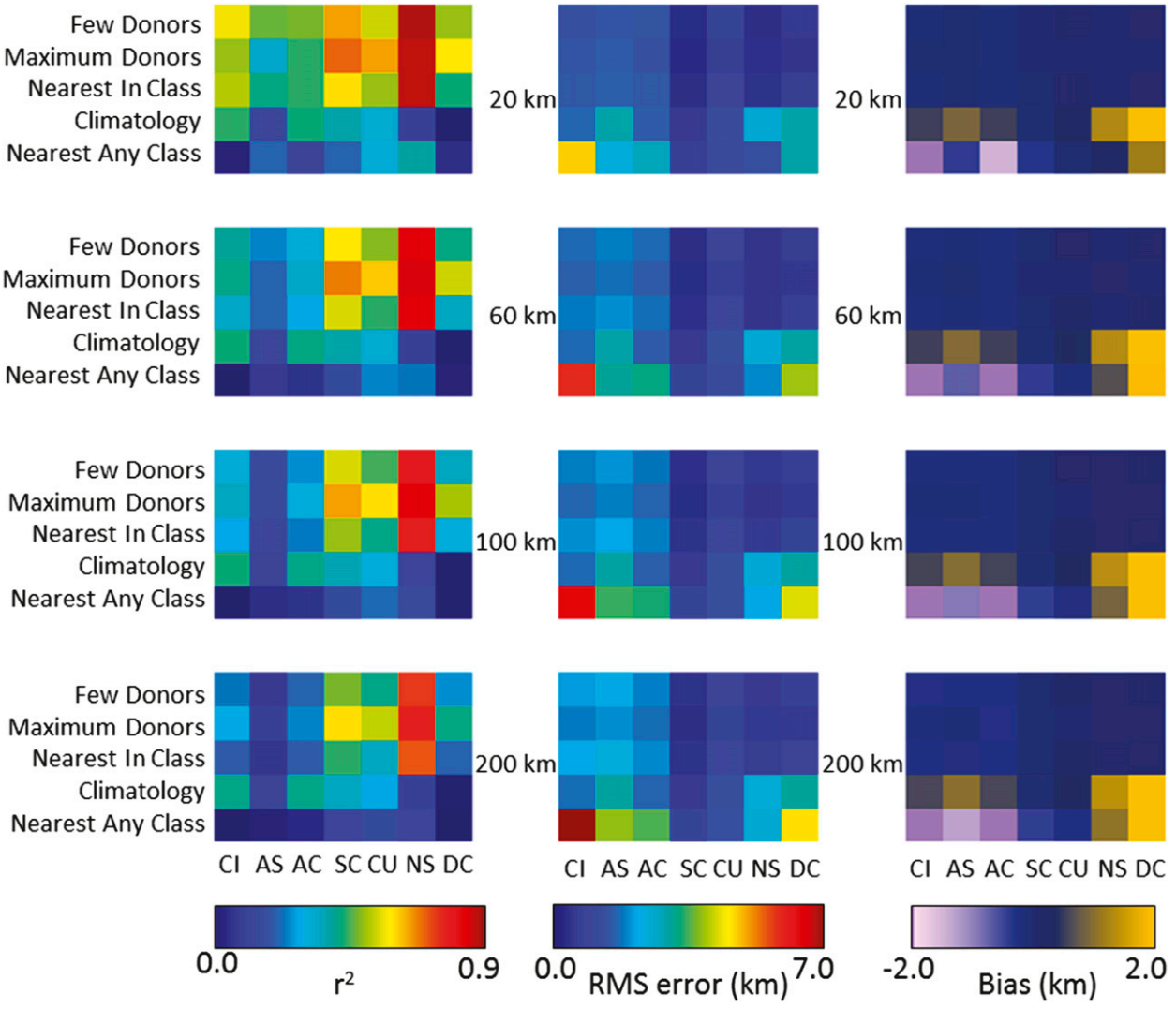

FIG. 6. Statistical results of data-exclusion experiment for cloud-base heights. The four rows correspond to increasing exclusion distances (20, 60, 100, and 200 km), and the three columns show (left to right) correlation (r^2), RMS error, and bias (estimated − observed), respectively. Within each panel, the four prediction methods (as illustrated in Fig. 5) and the seven 2B-CLDCLASS types studied are labeled.

some estimates, particularly the nearest neighbor of any type method where high clouds exist in close proximity to low clouds, as illustrated with the CI and SC in Fig. 5b. In the implementation of a cloud-base estimation technique to passive sensor satellite observations, there exist a number of ways to accurately estimate the cloud top (e.g., Kidder and Vonder Haar 1995).

Results of the data-exclusion experiment are shown in Fig. 6. The four rows correspond to exclusion distances; from top to bottom they are 20, 60, 100, and 200 km. The three panels in each row correspond to the correlation (r^2), the RMS error, and the bias for the exclusion distance. Within each panel, a 4 × 7 display of values is shown. These are the five prediction methods discussed above and illustrated in Fig. 5. The hypothesis is that the upper two rows in each panel of Fig. 6, representing the statistical algorithm developed here, should outperform the remaining rows of that panel. Notable attributes of Fig. 6 include the following:

1) The type-constrained prediction methods (few donors, maximum donors) and nearest neighbor of same type exhibit higher r^2 and lower RMS error than nearest neighbor of any type or climatology. This is true at all exclusion distances for SC, CU, NS, and DC, and at 20 km for CI, AS, and AC. Beyond 60 km for CI, AS, and AC, r^2 for any prediction method is less than 0.5, denoting poor performance.

Climatology is competitive for CI, AS, and AC at these ranges.

2) Nearest neighbor of any cloud type is never the top performer. The findings are consistent with Forsythe et al. (2000), who show that type-constrained techniques outperform distance-based techniques. While the nearest neighbor of any type may on occasion include predictions of the same type as the recipient, it is vulnerable to large errors because of contamination by clouds of other types.
3) For the DC and NS cloud types, climatology fares poorly for all ranges and exhibits a large positive bias (estimated minus observed; meaning that the climatological geometric thickness is too small, resulting in base height estimates that are too high). Alternative methods, such as a model-derived convective of lifting condensation level, may be more appropriate to use here.
4) Performance varies dramatically by cloud type. The SC, CU, NS, and DC types all show overall better performance than CI, AS, and AC. A characteristic shared by these types is the tendency for their cloud bases to reside in the lower atmosphere and occur uniformly over a region—lending themselves to better prediction when the true base height is known for even a small a subset of these clouds. The bias is reduced by the few donors, maximum donors, and nearest neighbor of the same type methods in comparison to the climatology and nearest neighbor of any type methods.

The performance difference between few donors and maximum donors is informative. Few donors was expected to perform better at low exclusion distances, since only a few relatively close proximity points of the same cloud type were used [Eq. (3)]. For the cloud types that typically have more nonuniform bases (CI, AS, and AC), few donors does outperform *maximum donors* at the 20-km exclusion distance. However, the maximum donors method has equal or better performance for SC, CU, NS, and DC. These are the cloud types with more uniform bases, and they decorrelate spatially more slowly than CI, AS, or AC (Fig. 3). The findings suggest that a cloud type and range-dependent blend of the few donors and maximum donors methods could optimize performance.

Homing in further on improvements of the current algorithm to the nearest neighbor of same cloud-type method, Fig. 7 extracts from Fig. 6 the correlation coefficients as a function of the *CloudSat* along-track exclusion distance for the CI and CU cloud types. The fact that nearest neighbor of same type is never the top performer is noteworthy. Whereas this method may provide superior prediction for clouds in very close proximity to the recipient cloud location (and likely part of the same cloud object), this assumption begins to fall apart for remote and unconnected clouds. As the standard deviation increases with distance, reasons to assume that the nearest member of a suite of possible donors will always provide the most representative estimate at the recipient location are less intuitive. The few donors method strikes a compromise, reducing the number of donors with decreasing range to the recipient, but expanding the number of donors as the range increases to provide a more diverse sampling of regional clouds of that type.

Also noteworthy in Fig. 7 is the cloud-type-dependent dichotomy of the two statistical algorithms. For CI, the few donors technique outperforms maximum donors at close range, but then gives way to maximum donors at longer ranges. In contrast, for CU the maximum donors technique prevails at all ranges. Consideration for the characteristic scale of CU and CI is helpful in explaining these differences; the slower varying nature of CI in contrast to CU means that closer-proximity donors are indeed more representative of the recipient. For CU, whose horizontal scale is typically much finer than CI, we rapidly enter a regime with increasing range where a greater sampling of donors yields the best result. As such, the selection of few donors and maximum donors should be made in the context of cloud type and range.

c. Application to 3D cloud rendering

To use cloud classification as a statistical constraint for estimating cloud vertical structure, we require a uniform definition for cloud type throughout the scene. The *CloudSat* 2B-CLDCLASS cloud types are based in part on the radar profile information itself, which is not available throughout the MODIS swath. The possible approaches for cloud-type reconciliation between *CloudSat* and MODIS include (i) developing trace statistics based on MODIS-derived cloud types [e.g., the algorithm of Pavolonis et al. (2005)] and (ii) mapping the *CloudSat*-derived cloud types to those derived from MODIS (e.g., Bankert et al. 2009) via a contingency table approach. Here, we illustrate how the latter approach can be applied to estimating the 3D characteristics of a tropical cyclone. The axially symmetric nature and notionally understood structure of these storms make them suitable for demonstrating the current algorithm in the context of the limited, linearly oriented sampling strategy of *CloudSat* curtain observations. In the more general application of this 3D algorithm, the active sensor observations may be spatially distributed,

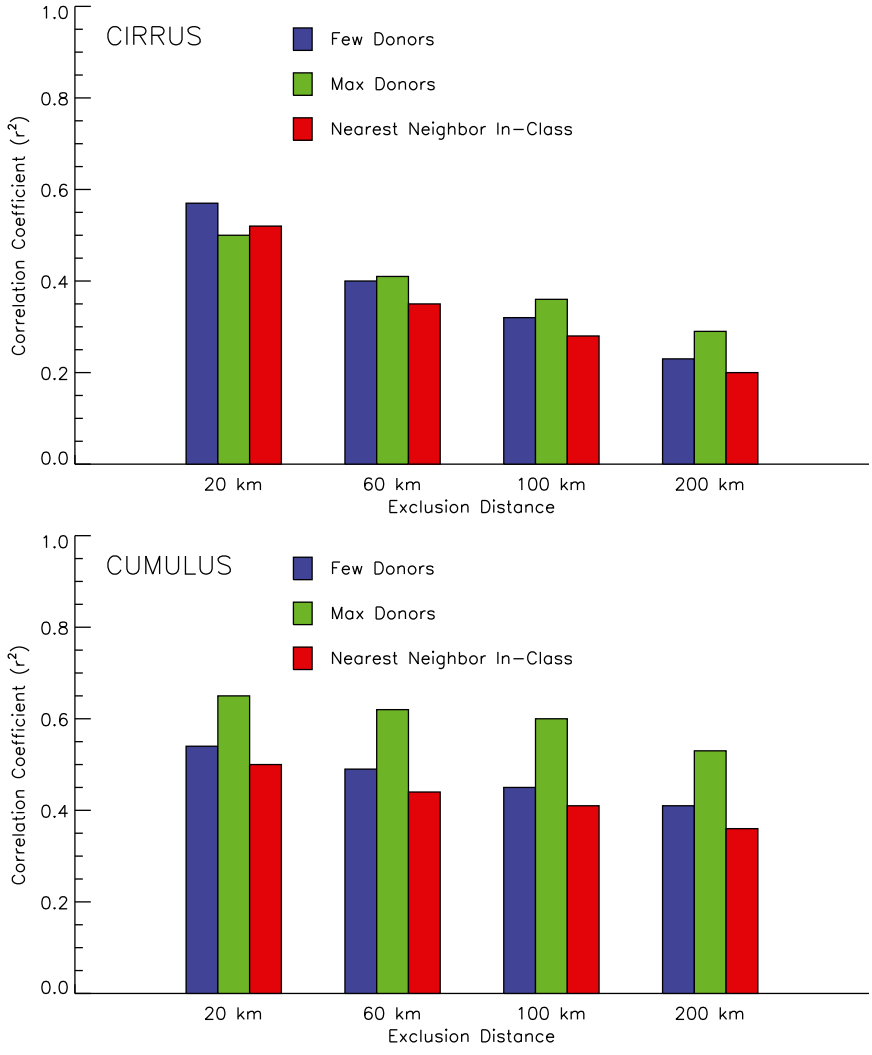

FIG. 7. Comparison of the correlation coefficient for cloud-base-height estimates using the methods of few donors, maximum donors, and nearest neighbor of same cloud type for (top) CI and (bottom) CU cloud types, shown as a function of exclusion distance.

and afford improved capability to estimate a variety of more complex–asymmetric cloud distributions.

The frequency of occurrence of each of the eight *CloudSat*-defined (2B-CLDCLASS) types corresponding to the six cloud types of Pavolonis et al. (2005) applied to MODIS data was constructed for July 2009. The analysis was performed for daytime observations from 432 orbits of collocated *CloudSat* and *Aqua* MODIS data. We enforced the constraint that each segment must contain a consistent cloud type over 20 fields of view (FOVs) (~22 km) in length, to focus our attention on the most contiguous data at the expense of heterogeneous scenes. To ensure consistency with what the passive MODIS observations are capable of sensing, only the 2B-CLDCLASS type corresponding to the uppermost cloud layer was used.

The resulting contingency matrix (Table 2) relates the 2B-CLDCLASS and MODIS-derived cloud types. Table 2 shows that MODIS partly cloudy types map most frequently into the 2B-CLDCLASS clear type.

TABLE 2. Mapping of MODIS cloud types to the 2B-CLDCLASS cloud types based on the July 2009 statistics.

	2B-CLDCLASS Type							
MODIS Type	Clear	CI	AS	AC	SC	CU	NS	Deep
Partly cloudy	15	0	1	4	0	0	0	0
Liquid	1985	238	58	260	3586	242	91	4
Supercooled	55	128	107	208	514	40	109	23
Opaque ice	0	78	368	0	7	4	86	460
Cirrus	196	2606	1031	91	11	7	303	103
Overlap	0	288	70	8	2	0	5	12

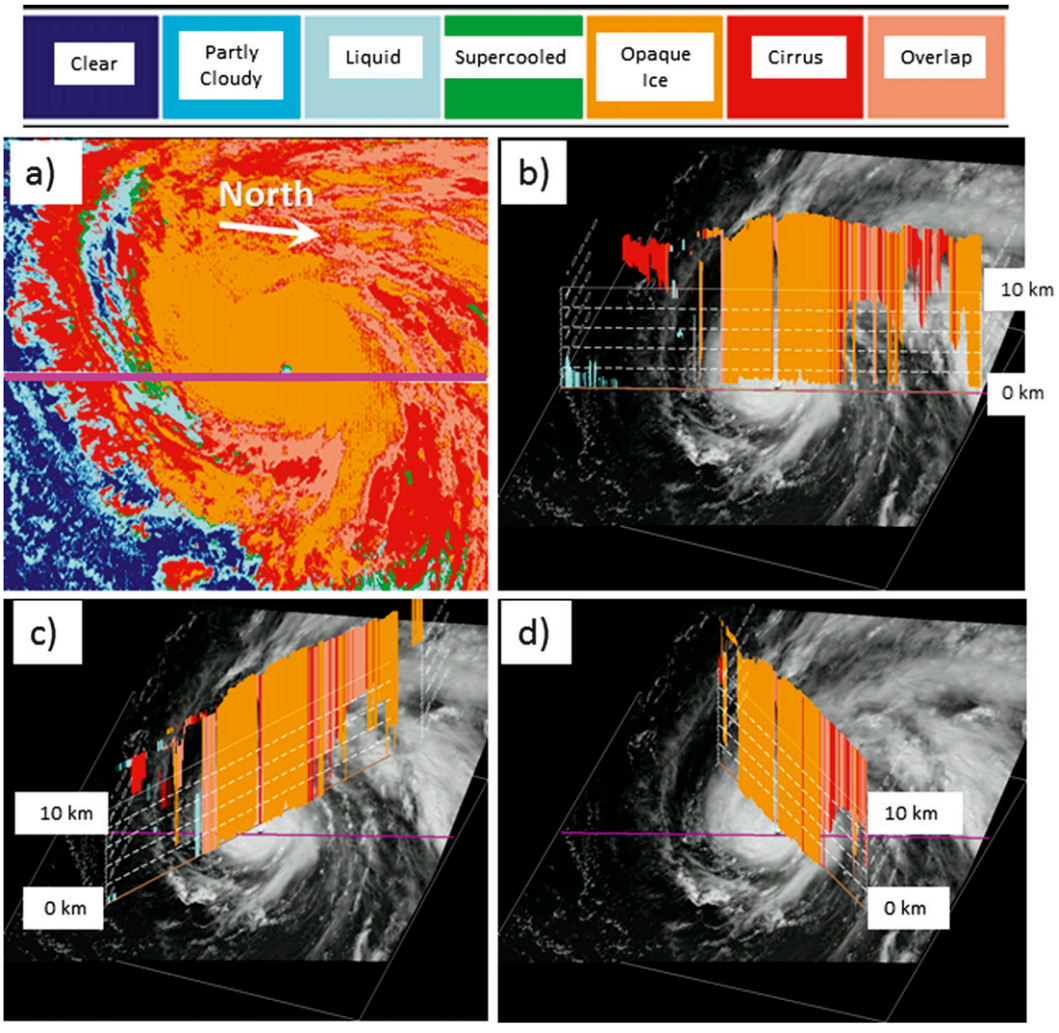

FIG. 8. Example of 3D cloud-field generation for Super Typhoon Choi-Wan, 0353 UTC 15 Sep 2009. (a) The MODIS cloud classification; the *CloudSat* ground track is shown by the purple line, and north is indicated by the arrow. (b) The MODIS visible image. The vertical extent of the uppermost cloud layer only is shown, as measured by *CloudSat*. Dashed lines are at 2-km intervals up to 10 km. The colors on the cross section correspond to the MODIS cloud type at cloud top from (a). (c),(d) The uppermost cloud layer is reconstructed along a line (brown) at two different oblique angles to the *CloudSat* track, respectively.

MODIS liquid water most often occurs in the 2B-CLDCLASS SC and clear types. Supercooled liquid clouds map most often to SC but also occur in AC, AS, and CI. Opaque ice maps primarily to DC but also maps to AS. The mappings between CI from each classifier are in fair agreement. The MODIS overlap cloud type detects thin ice cloud over a lower liquid cloud (Pavolonis and Heidinger 2004), and it is encouraging that it is strongly associated with CI (recalling that for *CloudSat* we selected the uppermost cloud-layer type).

The *CloudSat*–MODIS cloud-type mapping was used to enable 3D scene construction. We considered a direct pass of the A-Train over the eye of Super Typhoon Choi-Wan in the east Pacific, which occurred at 0352 UTC 15 September 2009 (Lee et al. 2012). Figure 8 illustrates the cloud typing, the measured *CloudSat* cloud profile along track, and two predictions of cloud geometric boundaries for the uppermost layer for arbitrary cross sections through the storm. Here, MODIS-derived cloud-top height constrains cloud top, and the cloud base is derived by the few donors method. Figure 8a shows the *CloudSat* track overlaid upon the MODIS classification. The core of Choi-Wan was classified as opaque ice, with CI and overlap cloud types emerging away from the typhoon center. Broken liquid clouds were detected far away from the core of the storm. In Fig. 8b, the MODIS visible image serves as a backdrop for the measured cloud profile from the active sensor data for the uppermost cloud

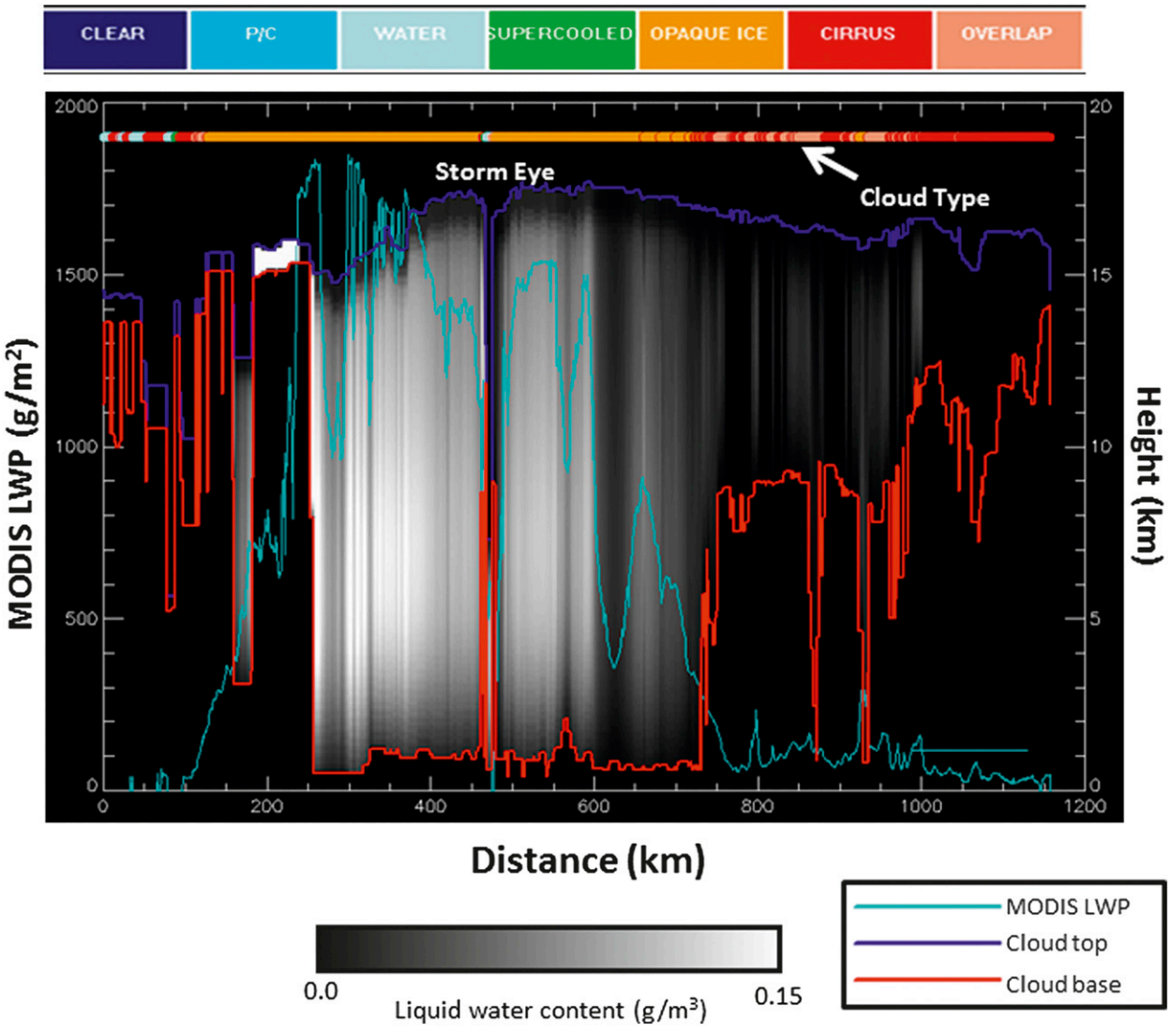

FIG. 9. Synthesized cloud water content profile along the cross section in Fig. 8d through Super Typhoon Choi-Wan. The MODIS liquid water path and top and the estimated base of the uppermost cloud layer are shown in light blue, dark blue, and red lines respectively. The MODIS cloud type through this cross section is indicated by the colored bar along 19-km height. Gray shadings indicate the estimated liquid water content profile using the full mission statistics and the reconciliation between MODIS and 2B-CLDCLASS cloud types.

layer only. The profile is colored according to the MODIS cloud type at cloud top. In general, the opaque ice cloud type is present with deep convection, while CI and overlap occur with thinner layers of cloud with bases above 8 km. A few liquid clouds with tops below 4 km are also indicated.

Estimated cross sections of the uppermost cloud layer away from the *CloudSat* track are shown in Figs. 7c and 7d. These arbitrarily selected cross sections were created with the type-dependent statistics, the maximum donors technique, and the MODIS–2B-CLDCLASS cloud-type reconciliation shown in Table 2. The deep convective core of the storm is represented in each cross section by the opaque ice type. Thinner cirrus and overlap types with tops between 10 and 15 km occur farther away from the storm center. Additional deep convection is detected in Fig. 8c in an outer band, well beyond the core of the storm. Cloud top for this illustration was estimated using the same method as base height estimation, although MODIS-retrieved information was also available.

To estimate the internal structure of these clouds and complete the 3D structural estimate, we combined the cloud-top height and integrated water path (provided by MODIS) with the cloud-base height estimated from our algorithm. The integrated water was converted into a profile of cloud water content using the cloud-type-dependent normalized water content profiles shown in Fig. 4. The result of this process is shown in Fig. 9,

corresponding to the estimated cross section of Fig. 8d. The estimated base and top are shown as red and dark blue lines, respectively. The MODIS-retrieved liquid water path (LWP) from the standard MOD06 cloud product is shown as a light blue line. The MODIS-derived cloud types are shown in color across the profile. The cross section passes through the relatively clear eye of Choi-Wan, as indicated by a local minimum in liquid water path adjacent to drastic increases in the eyewall. The estimated CWC profile is shown in grayscale. The structures are reminiscent of Fig. 4 distributions in most areas, although some issues emerge around ground-track distance of 200 km, where discrepancies in cloud-base-height assignment result in the ''packing'' of significant liquid water path within a vertically constrained geometric thickness.

6. Conclusions and future work

A statistically based technique for estimating 3D cloud structure from conventional 2D passive satellite imagery and limited vertical structure information was developed. At the heart of this quantitative approach is a simple premise that appeals to the earliest rationales for qualitative cloud classification, as first articulated by Howard (1802): the notion that cloud types, as ''birds of a feather,'' share quantitatively expressible attributes. Through its simple conditioning of statistics upon cloud type (which implicitly conditions upon a limited range of optical, microphysical, and geometric properties characteristic of each cloud type), the algorithm provides a straightforward method for myriad applications ranging from simple visualizations for flight-training software or virtual globes such as Google Earth, and evaluation of NWP model cloud structures, to cloud entrainment and 3D radiative transfer studies. With that said, we caution against using the 3D structures rendered by this algorithm as a form of truth for model verification.

This research illustrates the general utility of the satellite ''train'' constellations in exploiting multisensor observations in a synergistic way. The analysis suggests that cloud-type dependency yields improved performance over nearest-neighbor estimates ignorant to cloud type, as well as to climatological estimates. The current algorithm outperforms *climatology* and type-independent nearest neighbor methods at the 200-km range. Less skill was realized for the higher-level clouds (CI/AS/AC), but the algorithm outperformed the benchmark methods out to about the 60-km range. A full 3D cloud construction remains possible beyond these ranges using the current algorithm, but the estimates would not necessarily provide skill beyond that of *climatology*.

There are inherent limitations to the *CloudSat* observing system. There are problems with the detection of low clouds because of surface clutter. Limitations in radar sensitivity also result in the missing of some low clouds as well as thin cirrus. The CPR's sensitivity to precipitation-sized hydrometeors can in some cases obscure true cloud bases, lending to a possible confusion for precipitating cloud types (e.g., NS, DC, and some CU and SC). This sensitivity may also bias low the cloud water content profile structures derived from global *CloudSat* data for these same cloud types.

In terms of future research, use of other information to gain insight on cloud similarity may very well improve performance for particular cloud types, geographic regions, or seasons. Such methods include (i) using direct measurements of brightness temperature and visible reflectance (e.g., Barker et al. 2011), (ii) enlisting retrieved cloud optical depth, retrieved particle size, and cloud-type-dependent water content assumption (e.g., Hutchison et al. 2006), or (iii) including information from NWP model fields or other sensor data that characterize airmass regimes. Whereas the introduction of multiple conditions provides a way of homing in on maximal similarity, doing so comes at the expense of increased dimensionality and a need for considerably more observations to build robust statistical relationships.

There are additional tests that could be implemented with either the few donors or maximum donors methods to potentially improve their performance in specific situations. The spatial structure and contiguity of the donor points to the recipient point (e.g., members of the same cirrus shield) might be a useful indicator of a consistent, predictable cloud layer. The variability of the donor points themselves could be indicative of the complexity and hence the predictability of the recipient point. In some cases this variability may reflect the complexity of a particular meteorological situation, such as the interface between two different air masses. In other cases the variability may arise from dubious auxiliary information. For example, donor points identified as DC but possessing a large variation of base heights are more likely to be misclassified points and should not be used. Such self-diagnosing quality-control metrics could be used to apply the current technique only where the expected confidence is high.

In ongoing research, direct comparisons will be made against the VIIRS cloud-base-height retrieval, which enlists the Hutchison et al. (2006) approach. We also plan to augment these statistics with *CALIPSO* observations, which have recently become available. Doing so should improve cirrus statistics based on superior lidar detection, but additional information is limited for optically thick clouds because of attenuation (e.g., Miller and Stephens 1999). Enlisting *CALIPSO* will enable application of the method to aerosol parameters such as

mineral dust layers and 3D estimates of such features as the Saharan air layer (e.g., Prospero and Carlson 1972; Dunion and Velden 2004).

Acknowledgments. We gratefully acknowledge the time invested by our reviewers in helping us to improve this manuscript. This research was supported by the Naval Research Laboratory through Contract N00173-10-C-2003, the Oceanographer of the Navy through the Program Executive Office C4I/PMW-120 under Program Element PE-0603207N, the DoD Center for Geosciences/Atmospheric Research at Colorado State University under Cooperative Agreement W911NF-06-2-0015 with the Army Research Laboratory, and NASA Grant NNX09AN79G.

REFERENCES

Arakawa, A., 1975: Modeling clouds and cloud processes for use in climate models. *The Physical Basis of Climate and Climate Modelling,* GARP Publications Series 16, ICSU/WMO, 181–197.

Aumann, H. H., and Coauthors, 2003: AIRS/AMSU/HSB on the *Aqua* mission: Design, science objectives, data products, and processing systems. *IEEE Trans. Geosci. Remote Sens.,* 41, 253–264.

Austin, R. T., A. J. Heymsfeld, and G. L. Stephens, 2009: Retrieval of ice cloud microphysical parameters using the *CloudSat* millimeter-wave radar and temperature. *J. Geophys. Res.,* 114, D00A23, doi:10.1029/2008JD010049.

Bankert, R., C. Mitrescu, S. D. Miller, and R. H. Wade, 2009: Comparison of GOES cloud classification algorithms employing explicit and implicit physics. *J. Appl. Meteor. Climatol.,* 48, 1411–1421.

Barker, H. W., M. P. Jerg, T. Wehr, S. Kato, D. P. Donovan, and R. J. Hogan, 2011: A 3D cloud-construction algorithm for the EarthCARE satellite mission. *Quart. J. Roy. Meteor. Soc.,* 137, 1042–1058.

Baum, B. A., and Coauthors, 1995: Satellite remote sensing of multiple cloud layers. *J. Atmos. Sci.,* 52, 4210–4230.

Brenguier, J. L., and Coauthors, 2000: An overview of the ACE-2 CLOUDYCOLUMN closure experiment. *Tellus,* 52B, 815–827.

Dunion, J. P., and C. S. Velden, 2004: The impact of the Saharan air layer on Atlantic tropical cyclone activity. *Bull. Amer. Meteor. Soc.,* 85, 353–365.

Forsythe, J. M., T. H. Vonder Haar, and D. L. Reinke, 2000: Cloud base height estimates using a combination of meteorological satellite imagery and surface reports. *J. Appl. Meteor.,* 39, 2336–2347.

Haynes, J. M., C. Mitrescu, and G. L. Stephens, 2005: A combined lidar and radar retrieval of cloud optical properties. *Lidar Remote Sensing for Industry and Environmental Monitoring V,* U. N. Singh and K. Mizutani, Eds., International Society for Optical Engineering (SPIE Proceedings, Vol. 5653), doi:10.1117/12.578929.

Hogan, R. J., and S. F. Kew, 2005: A 3D stochastic cloud model for investigating the radiative properties of inhomogeneous cirrus clouds. *Quart. J. Roy. Meteor. Soc.,* 131, 2585–2608.

Holton, J. R., 1992: *An Introduction to Dynamic Meteorology.* 3rd ed. Academic Press, 511 pp.

Howard, L., 1802: *On the Modification of Clouds.* J. Taylor, 37 pp.

Hutchison, K., E. Wong, and S. C. Ou, 2006: Cloud base heights retrieved during night-time conditions with MODIS data. *Int. J. Remote Sens.,* 27, 2847–2862.

Kahn, B. H., and Coauthors, 2008: Cloud type comparisons of AIRS, *CloudSat*, and *CALIPSO* cloud height and amount. *Atmos. Chem. Phys.,* 8, 1231–1248.

Kidder, S. Q., and T. H. Vonder Haar, 1995: *Satellite Meteorology: An Introduction.* Academic Press, 466 pp.

King, M. D., Y. J. Kaufman, W. P. Menzel, and D. Tanré, 1992: Remote-sensing of cloud, aerosol, and water-vapor properties from the Moderate Resolution Imaging Spectroradiometer (MODIS). *IEEE Trans. Geosci. Remote Sens.,* 30 (10), 2–27.

King, N. J., and G. Vaughan, 2012: Using passive remote sensing to retrieve the vertical variation of cloud droplet size in marine stratocumulus: An assessment of information content and the potential for improved retrievals from hyperspectral measurements. *J. Geophys. Res.,* 117, D15206, doi:10.1029/2012JD017896.

L'Ecuyer, T. S., and J. H. Jiang, 2010: Touring the atmosphere aboard the A-Train. *Phys. Today,* 63, 36, doi:10.1063/1.3463626.

Lee, T. F., R. L. Bankert, and C. Mitrescu, 2012: Meteorological education and training using A-Train profilers. *Bull. Amer. Meteor. Soc.,* 93, 687–696.

Liu, G., J. A. Curry, and R.-S. Sheu, 1995: Classification of clouds over the western equatorial Pacific Ocean using combined infrared and microwave satellite data. *J. Geophys. Res.,* 100, 13 811–13 826.

Lynch, D. K., K. Sassen, D. Starr, and G. Stephens, Eds., 2002: *Cirrus.* Oxford University Press, 480 pp.

Menzel, W. P., and J. F. W. Purdom, 1994: Introducing GOES-I: The first of a new generation of geostationary operational environmental satellites. *Bull. Amer. Meteor. Soc.,* 75, 757–781.

Miller, S. D., and G. L. Stephens, 1999: Multiple scattering effects in the lidar pulse stretching problem. *J. Geophys. Res.,* 104 (D18), 22 205–22 219.

——, ——, and R. T. Austin, 2001: *GOES 10* cloud optical property retrievals in the context of vertically varying microphysics. *J. Geophys. Res.,* 106 (D16), 17 981–17 995.

Nakajima, T. Y., and M. D. King, 1990: Determination of the optical thickness and effective particle radius of clouds from reflected solar radiation measurements. Part I: Theory. *J. Atmos. Sci.,* 47, 1878–1893.

Pandey, P. C., E. G. Njoku, and J. W. Waters, 1983: Inference of cloud temperature and thickness by microwave radiometry from space. *J. Climate Appl. Meteor.,* 22, 1894–1898.

Pavolonis, M. J., and A. K. Heidinger, 2004: Daytime cloud overlap detection from AVHRR and VIIRS. *J. Appl. Meteor.,* 43, 762–778.

——, ——, and T. Uttal, 2005: Daytime global cloud typing from AVHRR and VIIRS: Algorithm description, validation, and comparisons. *J. Appl. Meteor.,* 44, 804–826.

Platnick, S., 2000: Vertical photon transport in cloud remote sensing problems. *J. Geophys. Res.,* 105 (D18), 22 919–22 935.

Prospero, J. M., and T. N. Carlson, 1972: Vertical and areal distributions of Saharan dust over the western equatorial North Atlantic Ocean. *J. Geophys. Res.,* 77, 5255–5265.

Ramanathan, V., and W. Collins, 1991: Thermodynamic regulation of ocean warming by cirrus clouds deduced from observations of the 1987 El Niño. *Nature,* 351, 27–32.

Randall, D. A., 1989: Cloud parameterization for climate models: Status and prospects. *Atmos. Res.,* 23, 345–362.

Stephens, G. L., 2003: The useful pursuit of shadows. *Amer. Sci.,* 91, 442–449.

——, and Coauthors, 2002: The *CloudSat* mission and the A-Train: A new dimension of space-based observations of clouds and precipitation. *Bull. Amer. Meteor. Soc.,* 83, 1771–1790.

——, P. J. Webster, R. H. Johnson, R. Engelen, and T. S. L'Ecuyer, 2004: Observational evidence for the mutual regulation of the tropical hydrological cycle and tropical sea surface temperatures. *J. Climate,* 17, 2213–2224.

Stowe, L. L., P. A. Davis, and E. P. McClain, 1999: Scientific basis and initial evaluation of the CLAVR-1 global clear/cloud classification algorithm for the Advanced Very High Resolution Radiometer. *J. Atmos. Oceanic Technol.,* 16, 656–681.

Tiedtke, M., 1993: Representations of clouds in large-scale models. *Mon. Wea. Rev.,* 121, 3040–3061.

Venema, V., and Coauthors, 2006: Surrogate cloud fields generated with the iterative amplitude adapted Fourier transform algorithm. *Tellus,* 58A, 104–120.

Wallace, J., 1992: Effect of deep convection on the regulation of tropical sea surface temperature. *Nature,* 357, 230–231.

Wang, X., K. Liou, S. S. Ou, G. Mace, and M. Deng, 2009: Remote sensing of cirrus cloud vertical size profile using MODIS data. *J. Geophys. Res.,* 114, D09205, doi:10.1029/2008JD011327.

Wang, Z., and K. Sassen, 2007: Level 2 cloud scenario classification product process description and interface control document. Version 5.0, Cooperative Institute for Research in the Atmosphere, 50 pp. [Available online at http://www.cloudsat.cira.colostate.edu/ICD/2B-CLDCLASS/2B-CLDCLASS_PDICD_5.0.pdf.]

Wielicki, B. A., B. R. Barkstrom, E. F. Harrison, R. B. Lee, G. L. Smith, and J. E. Cooper, 1996: Clouds and the Earth's Radiant Energy System (CERES): An Earth Observing System experiment. *Bull. Amer. Meteor. Soc.,* 77, 853–868.

Winker, D. M., and Coauthors, 2003: The *CALIPSO* mission: A global 3D view of aerosols and clouds. *Bull. Amer. Meteor. Soc.,* 91, 1211–1229.

Woods, C. P., D. E. Waliser, J.-L. Li, R. T. Austin, G. L. Stephens, and D. G. Vane, 2008: Evaluating *CloudSat* ice water content retrievals using a cloud-resolving model: Sensitivities to frozen particle properties. *J. Geophys. Res.,* 113, D00A11, doi:10.1029/2008JD009941.

Zhao, Q., and F. H. Carr, 1997: A prognostic cloud scheme for operational NWP models. *Mon. Wea. Rev.,* 125, 1931–1953.